Molecular-Orbital Framework of Two-Electron Processes: Application to Auger and Intermolecular Coulomb Decay

Nayanthara K. Jayadev^a, Wojciech Skomorowski^b, and Anna I. Krylov^a

^a Department of Chemistry, University of Southern California, Los Angeles, CA 90089, USA

^b Centre of New Technologies, University of Warsaw, Banacha 2c, 02-097 Warsaw, Poland

Abstract

States with core vacancies, which are commonly created by absorption of X-ray photons, can decay by a two-electron process in which one electron fills the core hole and the second one is ejected. These processes accompany many X-ray spectroscopies. Depending on the nature of the initial core-hole state and the decay valence-hole states, these processes are called Auger decay, intermolecular Coulomb decay, or electron-transfer-mediated decay. To connect many-body wavefunctions of the initial and final states with molecular orbital picture of the decay, we introduce a concept of natural Auger orbitals (NAOs). NAOs are obtained by two-step singular value decomposition of the two-body Dyson orbitals, reduced quantities that enter the expression of the decay rate in the Feshbach–Fano treatment. NAOs afford chemical insight and interpretation of the high-level ab intio calculations of Auger decay and related two-electron relaxation processes.

Molecular-orbital framework is of the central importance in chemistry as well as in atomic, molecular, and optical physics¹. Molecular orbitals explain bonding in molecules and mechanisms of chemical reactions. Molecular orbitals are also essential for understating light-matter interactions—they enable predictions of trends in spectroscopic cross-sections (e.g., absorption, fluorescence, and phosphorescence), angular-resolved quantities (polarization of the transitions, photoelectron angular distributions), and virbational lineshapes of various electronic transitions (e.g., Franck–Condon factors). Molecular orbitals determine experimental observables and, conversely, their shapes can be extracted from properly designed experimental measurements²⁻⁴. Hence, molecular orbitals are not just a mathematical construct—they represent physical reality that can be probed experimentally¹.

Theoretically, molecular orbitals can be derived from general many-body wave-functions¹,

and—contrary to the common misconception—are not restricted to low-level treatments, such as Hartree–Fock or Kohn–Sham density functional theories. The definition of appropriate orbitals depends on the type of a physical process rather than the electronic states themselves¹. That is, different observables give rise to different definitions of orbitals. For example, photo-ionization or photodetachment processes are described by Dyson orbitals^{5–10}, one-photon photoexcitation or emission are described by natural transition orbital (NTOs)^{11,12}, spin-forbidden processes such as phosphorescence, intersystem crossing, or magnetic anisotropy, give rise to spin–orbit NTOs¹³. Non-linear processes, such as two-photon (2PA) absorption, hyperpolarizabilities, and resonance inelastic X-ray scattering (RIXS) are described by the perturbed NTOs^{14–17}. A brief history of NTOs and related analyses is given in Ref. 1 (in particular, footnote 57).

FIG. 1: Essential information of a transition between the many-body initial and final states is contained in reduced quantities. Panel (a): Initial and final states in photoionization/photodetachment processes. These states are connected by one-electron Dyson orbital (the definition of the Dyson orbital amplitude is given on the right). Panel (b): Initial and final states in one-photon absorption processes. These states are connected by one-particle transition density matrix (equation on the right).

The definition of such physically relevant orbitals for many-body wave-functions is based on reduced quantities, such as reduced density matrices^{18–20}, that enter the expressions for the observables. Fig. 1a illustrates this idea for photoionization/photodetachment process. The key element entering the cross-section expression^{8,21} (called photoelectron matrix ele-

ment) can be written as a matrix element of the dipole operator between the Dyson orbital and the wave-function of the ejected electron. Dyson orbitals can be described as generalized overlap between the initial (N-electron) and final (N-1-electron) states:

$$\phi^{d}(x_{1}) = \sqrt{N} \int \Psi^{I}(x_{1}, x_{2}, \dots, x_{N}) \Psi^{F}(x_{2}, \dots, x_{N}) dx_{2} \dots dx_{N}$$
(1)

Using the Dyson amplitudes (shown in Fig. 1a), Dyson orbital can be expressed in terms of canonical Hartree–Fock molecular orbitals

$$\phi^d(x) = \sum_q \gamma_q \phi_q(x) \tag{2}$$

or any other set of orbitals used to represent the many-body wave-functions. The norms of Dyson orbitals, which quantify the one-electron character of the transitions, can be used in lieu of photoelectron intensities (pole strengths).

This simplification of the original expression—dipole matrix element between the two many-body wave-functions—is possible because electrons are indistinguishable and the integration can be carried out in two steps. Dyson orbitals describe the difference between the N and N-1 electron wave-functions and can be computed for wave-functions described by any level of theory, including the exact ones. Hence, they represent the generalization of canonical Hartree–Fock orbitals to a many-body framework^{1,10}.

Fig. 1b shows one-particle transition density matrix connecting the ground and excited states. This object contains all the information needed to compute the transition dipole moment for one-photon electronic transitions, such as those involved in UV-Vis or X-ray absorption or emission processes. The density matrix can be collapsed to the most compact form using singular value decomposition (SVD)

$$\gamma^{f \leftarrow i} = U \Sigma V^T \tag{3}$$

so that the transition density—often referred to as an exciton wave-function^{22–24}—can be represented as sum of pairs of hole and particle orbitals:

$$\rho^{tr}(x_p, x_h) = \sum_{rs} \gamma_{rs}^{f \leftarrow i} \phi_r(x_p) \phi_s(x_h) = \sum_K \sigma_K \psi_K^p(x_p) \psi_K^h(x_h), \tag{4}$$

where σ_K are singular values (elements of the diagonal matrix Σ , Eq. (3)), and

 $\psi_K^h(x_h)/\psi_K^p(x_p)$ are the corresponding hole and particle NTOs:

$$\psi_K^h(x) = \sum_{q} V_{qK} \phi_q(x), \tag{5}$$

$$\psi_K^h(x) = \sum_q V_{qK} \phi_q(x), \tag{5}$$

$$\psi_K^p(x) = \sum_q U_{qK} \phi_q(x). \tag{6}$$

The norm of γ , which can be evaluated as

$$||\gamma^{f \leftarrow i}|| = \sqrt{\sum_{K} \sigma_K^2},\tag{7}$$

quantifies one-electron character of the transition, similarly to the norms of Dyson orbitals. In molecules, typically only a small number of singular values are non-zero, whereas collective excitations (plasmons) are characterized by many contributions with similar weights. By using NTOs, intrinsic character of electronic transitions can be revealed and visualized.

The concept of NTOs was extended to spin-forbidden transitions by using spinless density matrices that enter the expressions of spin-orbit coupling between two multiplets¹³, to nonlinear properties, such as 2PA or RIXS, by using perturbed transition density matrices 14,15 , metastable electronic states 9,25 , and so on 16,17 .

FIG. 2: Initial and final states in regular (a) and resonant (b) Auger decay.

Here we introduce natural orbitals for two-electron processes, such as Auger-Meitner $decay^{26,27}$ and related phenomena—Interatomic Coulomb decay (ICD)²⁸ and electrontransfer-mediated decay (ETMD)²⁹. Auger decay accompanies many X-ray induced processes and entails filling a core vacancy by a valence electron with a simultaneous ejection of the second valence electron (Fig. 2). This is the main relaxation channel of core-excited or core-ionized states in molecules composed of light atoms. It is exploited in many spectroscopies and in applications (e.g., in radiotherapy and precision medicine^{30–33}). ICD and ETMD operate in a similar way, the only difference being that the core hole and the two electrons involved in the relaxation process belong to the two nearby molecules, for example, the two valence hole states in the final ICD state are located on two different molecules.

Although primary Auger processes—such as shown in Fig. 2—result in ejection of one electron, they cannot be described by the Dyson orbitals suitable for photoionization/photodetachment, Eq. (1). This is because Auger decay is an inherently two-electron processes—to connect the initial core-hole state and the final state, two electrons need to change their states (Fig. 2). Mathematically, it means that this transition requires three creation/annihilation operators, giving rise to two-body Dyson orbitals^{34–37}:

$$\Gamma_{qr}^p = \langle \Psi^F | p^\dagger q r | \Psi^I \rangle \tag{8}$$

$$\Gamma_r^{pq} = \langle \Psi^I | p^{\dagger} q^{\dagger} r | \Psi^F \rangle , \qquad (9)$$

where Ψ^I is the initial core-hole state and Ψ^F is the final state. In Hermitian theories, Γ^p_{qr} and Γ^{pq}_r are conjugates of each other, but in EOM-CC the two objects are distinct and both need to be computed for evaluation of decay rates³⁴. For non-resonant Auger decay (Fig. 2a) Ψ^I is a core-ionized state and Ψ^F is a valence doubly ionized state. For resonant Auger decay (Fig. 2b) Ψ^I is core-excited state and Ψ^F is the valence ionized state. To describe core-vacancy states, we use EOM-CCSD combined with with core-valence separation (CVS) scheme³⁸: CVS-EOM-IP CCSD for core-ionized states and CVS-EOM-EE-CCSD for core-excited states^{39–42}. The final decay states are described by EOM-DIP-CCSD (for non-resonant Auger) and EOM-IP-CCSD (for resonant Auger). Core electrons are frozen in the reference CCSD calculations.

Within the Feshbach–Fano treatment of metastable core-hole states³⁴, two-body Dyson orbitals enter the expression for computing the decay widths $(\tilde{\Gamma}_{\mu})$ of these states. In this treatment, CVS is used to define a projector operator, which separates the core-hole states from the continuum, making them bound with respect to electron loss. The decay channel is described by a product of doubly ionized molecular state times a free-electron state, described explicitly by a continuum function. The energy of Auger electrons is given by the energy difference between the core-hole state and target valence (doubly or singly) ionized state and the intensity of each decay channel is proportional to the corresponding $\tilde{\Gamma}_{\mu}$ (the width is inversely proportional to the decay rate and faster decay channels outcompete slower decay channels). The width of the core-hole state is given by the matrix element of

the Hamiltonian between the initial and final state, which reduces to:

$$\tilde{\Gamma}_{\mu} = 2\pi g_{\alpha} \int d\Omega_{\mathbf{k}} \left(\sum_{p} h_{p\mathbf{k}}{}^{\mu} \gamma^{p} + \frac{1}{2} \sum_{pqr} \langle pq | |\mathbf{k}r \rangle {}^{\mu} \Gamma_{r}^{pq} \right) \left(\sum_{p} h_{\mathbf{k}p}{}^{\mu} \gamma_{p} + \frac{1}{2} \sum_{pqr} \langle \mathbf{k}r | |pq \rangle {}^{\mu} \Gamma_{pq}^{r} \right),$$

$$(10)$$

where g_{α} is electronic degeneracy factor, index μ marks the decay channel (i.e., a particular final state), γ and Γ are respective one- and two-body Dyson orbitals, and $h_{\mathbf{k}r}$ and $\langle \mathbf{k}r||pq\rangle$ are one- and two-electron integrals with index \mathbf{k} denoting the free-electron state (represented by a continuum function) and indices p,q,r denoting bound molecular orbitals (represented by Gaussians). In this study, we represent the ejected electron state by the plane wave⁴³, but the formalism can be generalized to more sophisticated treatments.

Recently, this treatment was combined with the EOM-CCSD theory and applied to calculations of resonant and non-resonant Auger spectra^{34,43,44} as well as ICD⁴⁵. The theoretical background of this treatment and details of the implementation can be found in Ref. 34.

Here we use the two-particle Dyson orbitals, Eqns. (8) and (9), to define natural Auger orbitals (NAOs) that provide the most compact orbital picture of the Auger decay. Following the same strategy as in the derivation of NTOs, we use SVD to reduce the three-index tensor Γ to a small number of three-orbital sets. For Γ_r^{pq} defined by Eq. (9), index r corresponds to the core hole, and indices p and q—to the valence holes in the target state (see Fig. 2a). Hence, we first perform SVD on Γ_r^{pq} reshaped as $M \times M^2$ matrix, $\Gamma_{r,pq}$, where pq represents a combined index $p \times M + q$ and M is the number of molecular orbitals (specifically, we use $\beta \alpha \beta$ block; more on spin-symmetry below). As per Eqs. (3) and (5), this step yields the core NAO with its respective singular value. In the non-resonant Auger process, where the initial state has a single core vacancy, only one non-zero singular value is expected, however, in the resonant Auger decay, several core orbitals may be involved.

The core NAOs are given by the columns of matrix U, as per Eq. (5), and the corresponding columns of the matrix V contain the information about the decay NAOs, p and q. To compute them, we reshape the corresponding column of V into the $M \times M$ matrix and perform SVD on it. This step yields pairs of orbitals that describe the target decay states. As we show below, this step often yields several non-zero singular values, reflecting multi-configurational character of the target states. These NAOs represents a natural way to visualize the Auger decay and related processes (such as ICD and ETMD). Because Γ_r^{pq} enters the expression for decay widths, Eq. (10), the shapes of NAO can help to rationalize

the trends in $\tilde{\Gamma}_{\mu}$. For example, when Γ_r^{pq} is represented by a single set of three NAOs, one can evaluate their contribution to the decay width as follows:

$$\tilde{\Gamma}_{\mu} \approx \frac{\pi}{2} g_{\alpha} \left(\sigma^{1} \sigma^{2} \langle \psi^{p} \tilde{\psi}^{p} || \psi^{h} \mathbf{k} \rangle \right)^{2}$$
(11)

where σ^1 and σ^2 are the leading singular values from the first and the second SVD steps, respectively, ψ^h is the core-hole NAO from the first step, and ψ^p and $\tilde{\psi}^p$ are the two particle NAOs from the second SVD step.

As mentioned above, we use the $\Gamma_{r_{\beta}}^{p_{\alpha}q_{\beta}}$ block of Γ . In regular Auger calculations, the ionized core-hole is of β spin by default, so that $\Gamma_{r_{\alpha}}^{p_q}$ blocks are zero. For the target DIP states with $M_S=0$ (the default in Q-Chem), $\Gamma_{r_{\beta}}^{p_{\alpha}q_{\beta}}=\pm\Gamma_{r_{\beta}}^{p_{\beta}q_{\alpha}}$ for the triplet and singlet channels, respectively. Hence, for a closed-shell reference, using the $\Gamma_{r_{\beta}}^{p_{\alpha}q_{\beta}}$ block is equivalent to spin averaging. The second SVD procedure yields pairs of the decay NAOs corresponding to $\alpha\beta$ configurations (the σ values for $\alpha\beta$ and $\beta\alpha$ decay states are identical). To better understand the relationship between NAOs and the wavefunction amplitudes, we point out that the leading block of $\Gamma_r^{p_q}$ in regular Auger decay is³⁴:

$$\Gamma_K^{ij} \approx l_K r_{ii},$$
(12)

where l and r are left CVS-IP and right EOM-DIP amplitudes, respectively, K denotes core orbitals and i, j denote valence orbitals. Thus, the decay NAOs should roughly follow the DIP amplitudes.

In the resonant Auger process, assuming that the ejected electron has α -spin, $\Gamma_{r_{\beta}}^{p_{\beta}q_{\alpha}} = \Gamma_{r_{\alpha}}^{p_{\alpha}q_{\beta}} = \pm (\Gamma_{r_{\alpha}}^{p_{\alpha}q_{\beta}} = \Gamma_{r_{\alpha}}^{p_{\beta}q_{\alpha}}).$

Thus, the core-hole orbital for the first step has identical α and β components, but only β component is computed.

The leading blocks of Γ_r^{pq} in resonant Auger decay are³⁴:

$$\Gamma_J^{ai} \approx -l_J^a r_i, \tag{13}$$

$$\Gamma_K^{ij} \approx -\sum_a l_K^a r_{ij}^a,\tag{14}$$

where l and r are left CVS-EE and right EOM-IP amplitudes, respectively. Egns. (13) and (14) provide dominant contributions for the participator and spectator decay, respectively.

The renormalized σ^2 represent the weights of the particular configuration in the total wavefunction. A useful quantity is participation ratio (PR_{NTO}) , which quantifies how many orbitals (or orbital pairs) contribute to the wavefunction:

$$PR_{NTO} = \frac{(\sum_{K} \sigma_K^2)^2}{\sum_{K} \sigma_K^4}.$$
 (15)

For example, $PR_{NTO}=1$ when there is only one dominant amplitude for core-hole state, $PR_{NTO}=2$ for the two core hole states, and so on.

We implemented this procedure in the Q-Chem electronic structure package^{46,47} for non-resonant and resonant Auger decay. Additional details are given in the SI. We illustrate the utility of NAOs by application to water and benzene molecules, and a model solvated hydroxide cluster. All calculations are done using the Q-Chem electronic structure package⁴⁶. Q-Chem's symmetry notations are used⁴⁸.

TABLE I: Water.^a Ionization energies of the doubly ionized states (eV), energies of the Auger electrons (eV), partial decay widths (meV), the values of the leading DIP amplitudes, and PR_{NTO} s from the first and second SVD steps.

State	\mathbf{E}^{DIP}	E^b_{Auger}	$ ilde{\Gamma}$	Composition	PR_{NTO1}	PR_{NTO2}
$^{1}A_{1}$	41.58	498.56	17.72	$1b_2^{-2} (0.91), 3a_1^{-2} (0.19)$	1	1.10
3A_2	44.67	495.48	0.005	$1b_2^{-1}1b_1^{-1}\ (0.66)$	1	2.00
$^{1}\mathrm{B}_{1}$	48.76	491.39	13.46	$3a_1^{-1}1b_1^{-1} \ (0.67)$	1	2.00

^a MP2/aug-cc-pVTZ optimized structure; fully uncontracted 6-311(2+,+) G^{**} basis set was used for DIP and CVS EOM-IP. ^b Energies of Auger electrons computed using core IE of 540.15 eV.

Table I shows the three lowest decay channels for core-ionized water including their character based on the leading EOM-DIP-CCSD amplitudes (right vectors). The corresponding NAOs are shown in Fig. 3; their PR_{NTO} s are shown in Table I. As one can see, the singular values for the first step (that yields the initial core-hole state) are very close to one, giving rise to $PR_{NTO1}=1$. The shapes of the decay NAOs (orbitals from the second step) are similar to the canonical MOs, and their singular values and respective PR_{NTO} s are consistent with the leading amplitudes of the DIP states, as per Eq. (12). (Table I). For example, the PR_{NTO} s for $^{3}A_{2}$ and $^{1}B_{1}$ are close to two, consistent with $\alpha\beta$ and $\beta\alpha$ configurations of the DIP amplitudes. The DIP states derived from removing both electrons from the same

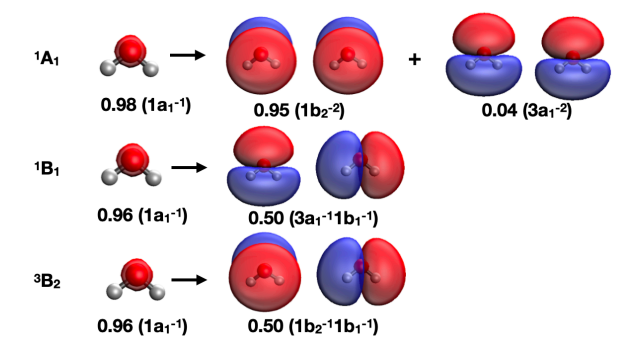


FIG. 3: Natural Auger Orbitals for the ${}^{1}A_{1}$, ${}^{1}B_{1}$, and ${}^{3}A_{2}$ decay channels of the ${}^{1}s_{O}$ -ionized state of water. Squared singular values from the first (left) and second (right) SVD steps are shown under the NAOs, along with the dominant electronic configurations (only $\alpha\beta$ decay NAOs are shown).

orbital give rise to one decay pair, whereas the DIP states derived by removing two electrons from different MOs give rise to two pairs of NAOs.

TABLE II: Benzene^a. Ionization energies of the doubly ionized states (eV), core-ionized states (eV), the corresponding energies of the Auger electrons^c (eV), partial decay widths (meV), the values of the leading DIP amplitudes, and PR_{NTO} s from the first and second SVD steps.

State	\mathbf{E}^{DIP}	core	\mathbf{E}^c	\mathbf{E}^d_{Auger}	$ ilde{\Gamma}$	Composition	PR_{NTO1}	PR_{NTO2}
$^{1}\mathrm{B}_{1g}$	25.40	$2a_g^{-1}$	291.20	265.80	0.130	$1b_{2g}^{-1}1b_{3g}^{-1}(0.66)$	1.11	2.01
$^{1}\mathrm{A}_{g}$	25.40	$2\mathbf{b}_{3u}^{-1}$	291.18	265.78	0.760	$1b_{2g}^{-2}(0.66),1b_{3g}^{-2}(0.66)$	1.12	2.01
$^3\mathrm{B}_{3g}$	27.75	$1\mathbf{b}_{2u}^{-1}$	291.24	263.50	0.003	$3b_{1g}^{-1}1b_{2g}^{-1} \ (0.47), \ 6a_g^{-1}1b_{3g}^{-1} \ (0.47)$	1.07	4.14
${}^{3}\mathrm{B}_{3u}$	27.80	$1\mathbf{b}_{1g}^{-1}$	291.20	263.40	0.001	$1b_{2g}^{-1}1b_{1u}^{-1}\ (0.67)$	1.05	2.00
$^{1}\mathrm{A}_{u}$	29.80	$1a_g^{-1}$	291.26	261.47	0.040	$4b_{2u}^{-1}1b_{2g}^{-1}\ (0.47),\ 5b_{3g}^{-1}1b_{3g}^{-1}\ (0.47)$	1.08	4.00

^a RI-MP2/cc-pVTZ optimized structure; 6-311G** basis set was used for DIP and CVS EOM-IP.

In contrast to water, benzene has six core orbitals and each can contribute to Auger decay. This, along with high symmetry of benzene, gives rise to a rich Auger spectrum^{49–51}, which we recently described theoretically⁴⁴. In the analysis below, we use the irreducible representations of D_{2h} point group, the largest Abelian subgroup of D_{6h} point group of benzene following the convention in Q-Chem. Here we focus on the NAO analysis of selected decay channels. Table II shows the energies of several doubly ionized states of benzene and their leading DIP amplitudes. Based on DIP amplitudes, the decay channels can be divided

into the three types: decay states corresponding to the ionization of doubly degenerate HOMO, decay states corresponding to ionization from HOMO and HOMO-1/HOMO-2, and decay states corresponding to the ionization from HOMO and HOMO-3.

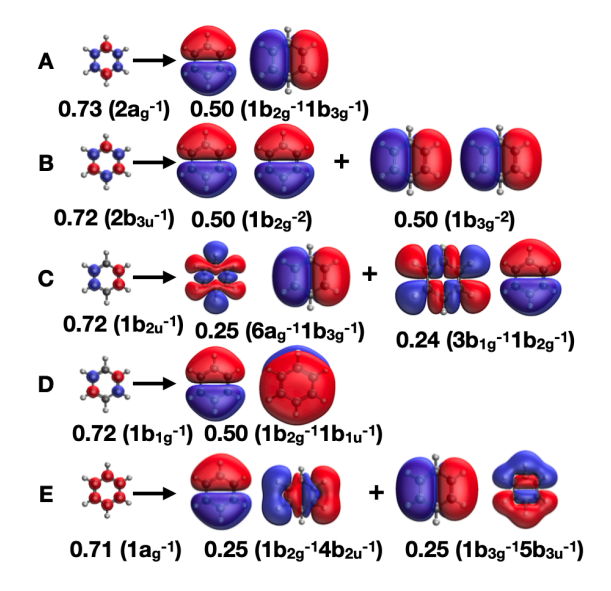


FIG. 4: Natural Auger Orbitals for selected decay channels in $1s_C$ -ionized benzene. Squared singular values from the first (left) and second (right) SVD steps are shown, along with the dominant electronic configurations (only $\alpha\beta$ decay NAOs are shown).

Fig. 4 shows the NAOs for the decay channels summarized in Table II. For this example, the shapes of NAOs appear to be similar to the shapes of canonical MOs. For decay channel (A), the first SVD yields a single singular value corresponding to the core-ionized $2a_g$ orbital. The second SVD shows that the main decay channel is derived by removal of electrons from the $1b_{2g}$ and $1b_{3g}$ HOMOs of benzene, consistent with the amplitudes of the ${}^{1}B_{1g}$ DIP state. Likewise, we see that channel (B) corresponds to the core hole of b_{3u} symmetry and two decay channels with either doubly ionized $1b_{2g}$ or doubly ionized $1b_{3g}$ HOMOs. The analysis shows that channels (C)-(E) correspond to ionization from the HOMO and lower orbitals. For this example, the NAO analysis closely follows the DIP amplitudes of the decay channels, and the shapes of NAOs are similar to those of the canonical Hartree–Fock MOs or the natural orbitals of the DIP states⁴⁴, however, the examples below illustrate that this is not always the case.

As the next example, we consider resonant Auger decay in benzene. The brightest peak in the XAS of benzene corresponds to the $1s_c \to \pi^*$ transition of B_{1u} symmetry (traditionally called A peak).^{52,53} In our calculations, this state appears at 286.9 eV. Consistent with the orbital degeneracy patterns, NTO analysis for this transition^{52,53} yields several pairs of NTOs (PR_{NTO} =2.45). Fig. 5 shows NAOs for Auger decay of this state. Consistent with XAS NTOs (see Fig. S1 in the SI), we obtain two core holes with equal weights and two decay NAOs, one of which is the π^* LUMO and the second is the a lower valence orbital (HOMO-1). The large σ^2 value for the second step reflects that EOM-IP decay state is dominated by a single valence hole. According to this picture, this decay channel corresponds to the participator decay. We note that in the resonant Auger decay one can consider an alternative definition of NAOs, i.e., by first doing SVD for $\Gamma_{rp,q}$. Such procedure yields NAOs that look like a union of NTOs for the XAS transition and a valence hole, as per Eq. (13); this is illustrated in Fig. S2 in the SI.

Finally, Fig. S3 in the SI shows NAOs for the spectator decay in benzene. We note that in this case the singular values are much smaller compared to the participator decay.

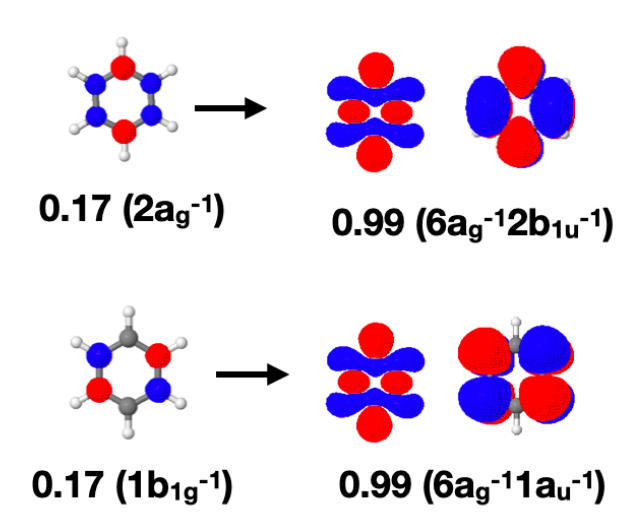


FIG. 5: Natural Auger Orbitals for resonant Auger decay in benzene. The initial state is B_{1u} core-excited state with excitation energy 286.9 eV (peak A in XAS). Squared singular values from the first (left) and second (right) SVD steps are shown, along with the dominant electronic configurations (only $\beta \to \alpha \beta$ NAOs are shown). The PR_{NTO} s from the first SVD is 2.51 consistent with the CVS EOM-EE amplitudes, and that from second SVD is 1.02 each corresponding to the single valence hole for every dominant core hole.

Our last example is a model cluster of hydroxide solvated with five water molecules (the

structure is taken from ab initio molecular dynamics equilibrium trajectory⁵⁴). We consider Auger decay of the core-ionized $1s_O$ state of hydroxide—this state has the lowest IE (534.02 eV) of the six $1s_O$ states of the cluster. Table III shows three lowest-energy singlet decay channels (corresponding to the fastest Auger electrons). In this case, the decay states can be either localized on hydroxide or on the nearby waters, or both. The DIP amplitudes (see Fig. S6 in the SI) involve many transitions, making the characterization of the decay channels difficult. In contrast, the NAO analysis yields much more compact picture. Fig. 6 shows NAOs for the three lowest singlet decay channel of the cluster. The analysis of the triplet decay channels is given in the SI. As one can see, all three channels have contributions both from the hydroxide orbitals and from the waters. The relative weight of the hydroxide is the largest in the first channel and the smallest in the third channel, which correlates with the computed decay widths that decrease in this sequence: 1 > 2 > 3. Based on the shapes of the NAOs, these three channels appear to be of mixed Auger and ICD decay character.

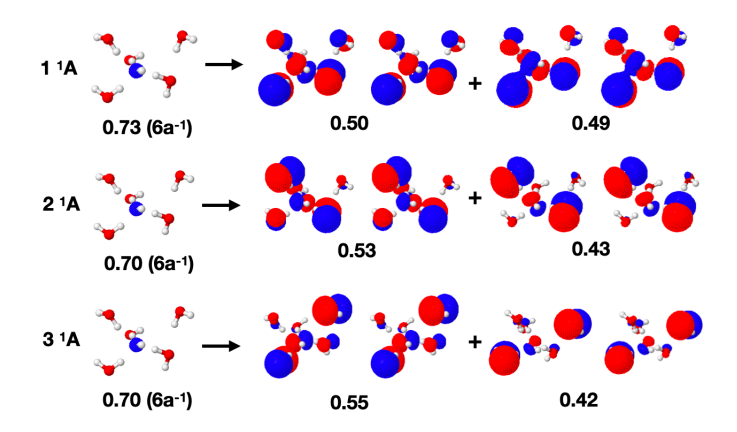


FIG. 6: Natural Auger Orbitals for the first three singlet decay channels of the $1s_O$ -ionized state of $OH^-(aq)$. Singular values from the first (left) and second (right) SVD steps are shown under the NAOs, along with the dominant electronic configurations.

In conclusion, we presented an extension of molecular orbital framework for two-electron processes such as Auger-Meitner decay or ICD. The theory is based on two-body Dyson orbitals connecting the initial (core-ionized or core-excited) and final states. Two sequential singular-value decompositions of the two-body Dyson orbitals yield a small number of three-orbital sets, which provide a compact representation of the decay process. This new tool enables casting of two-electron decay involving correlated many-body wave-functions into a simple yet rigorous molecular orbital picture thus facilitating analysis and providing insight

TABLE III: $OH^-(H_2O)_5$ cluster. Ionization energies of the singlet doubly ionized states (eV), energies of the Auger electrons (eV), partial decay widths (meV), and PR_{NTO} s from the first and second SVD steps.

State	\mathbf{E}^{DIP}	E_{Auger}	$ ilde{\Gamma}$	PR_{NTO1}	PR_{NTO2}
1^1 A	16.66	517.36	0.007	1	2.04
2^1 A	16.79	517.23	0.005	1	2.10
3^1 A	16.93	517.10	0.002	1	2.03

^a 6-311G basis set was used for DIP and CVS EOM-IP; core IE is 534.02 eV.

into X-ray induced processes.

Acknowledgments

We thank Dr. Pavel Pokhilko for his help with validating our implementation. This work was supported in Los Angeles by the U.S. National Science Foundation (No. CHE-2154482 to A.I.K.)

Conflicts of interest

The authors declare the following competing financial interest(s): A.I.K. is the president and a part-owner of Q-Chem, Inc.

- $^1\,$ Krylov, A. I. From orbitals to observables and back J. Chem. Phys. 2020, 153, 080901.
- ² Santra, R. Imaging molecular orbitals using photoionization *Chem. Phys.* **2006**, *329*, 357–364.
- ³ Puschnig, P.; Berkebile, S.; Fleming, A. J.; Koller, G.; Emtsev, K.; Seyller, T.; Riley, J. D.; Ambrosch-Draxl, C.; Netzer, F. P.; Ramsey, M. G. Reconstruction of molecular orbital densities from photoemission data *Science* 2009, 326, 702–706.
- Wei, S.; Lüftner, D.; Ules, T.; Reinisch, E. M.; Kaser, H.; Gottwald, A.; Richter, M.; Soubatch, S.; Koller, G.; Ramsey, M. G.; Tautz, F. S.; Puschnig, P. Exploring three-dimensional orbital imaging with energy-dependent photoemission tomography *Nat. Comm.* 2017, 6, 8287.
- ⁵ Goscinski, O.; Lindner, P. Natural spin-orbitals and generalized overlap amplitudes J. Math. Phys. 1970, 11, 1313–1317.
- ⁶ Linderberg, J.; Öhrn, Y. Propagators in quantum chemistry; Academic, London, 1973.
- Oana, C. M.; Krylov, A. I. Dyson orbitals for ionization from the ground and electronically excited states within equation-of-motion coupled-cluster formalism: Theory, implementation, and examples J. Chem. Phys. 2007, 127, 234106–14.
- ⁸ Gozem, S.; Gunina, A. O.; Ichino, T.; Osborn, D. L.; Stanton, J. F.; Krylov, A. I. Photoelectron wave function in photoionization: Plane wave or Coulomb wave? *J. Phys. Chem. Lett.* **2015**, 6, 4532–4540.
- ⁹ Jagau, T.-C.; Krylov, A. I. Characterizing metastable states beyond energies and lifetimes: Dyson orbitals and transition dipole moments J. Chem. Phys. 2016, 144, 054113.
- Ortiz, J. V. Dyson-orbital concepts for description of electrons in molecules J. Chem. Phys. 2020, 153, 070902.
- Luzanov, A. V.; Sukhorukov, A. A.; Umanskii, V. E. Application of transition density matrix for analysis of excited states *Theor. Exp. Chem.* 1976, 10, 354–361; Russian original: Teor. Eksp. Khim., 10, 456 (1974).
- ¹² Luzanov, A. V.; Pedash, V. F. Interpretation of excited states using charge-transfer number Theor. Exp. Chem. 1979, 15, 338–341.
- Pokhilko, P.; Krylov, A. I. Quantitative El-Sayed rules for many-body wavefunctions from spinless transition density matrices J. Phys. Chem. Lett. 2019, 10, 4857–4862.
- ¹⁴ Nanda, K. D.; Krylov, A. I. Visualizing the contributions of virtual states to two-photon ab-

- sorption cross-sections by natural transition orbitals of response transition density matrices J. Phys. Chem. Lett. **2017**, 8, 3256-3265.
- Nanda, K. D.; Krylov, A. I. A simple molecular orbital picture of RIXS distilled from many-body damped response theory J. Chem. Phys. 2020, 152, 244118.
- Nanda, K. D.; Krylov, A. I. The orbital picture of the first dipole hyperpolarizability from many-body response theory J. Chem. Phys. 2021, 154, 184109.
- ¹⁷ de Wergifosse, M.; Grimme, S. A unified strategy for the chemically intuitive interpretation of molecular optical response properties J. Chem. Theory Comput. 2020, 16, 7709–7720.
- ¹⁸ McWeeny, R. Methods of Molecular Quantum Mechanics; Academic Press, 2nd ed., 1992.
- ¹⁹ Mestechkin, M. M. Metod matritsy plotnosti v teorii molekul; Kyev, Naukova Dumka, 1977.
- Helgaker, T.; Jørgensen, P.; Olsen, J. Molecular electronic structure theory; Wiley & Sons, 1–944, 2000.
- ²¹ Gozem, S.; Krylov, A. I. The ezSpectra suite: An easy-to-use toolkit for spectroscopy modeling WIREs: Comput. Mol. Sci. **2022**, 12, e1546.
- ²² Bäppler, S. A.; Plasser, F.; Wormit, M.; Dreuw, A. Exciton analysis of many-body wave functions: Bridging the gap between the quasiparticle and molecular orbital pictures *Phys. Rev. A* 2014, 90, 052521.
- ²³ Mewes, S. A.; Plasser, F.; Krylov, A.; Dreuw, A. Benchmarking excited-state calculations using exciton properties *J. Chem. Theory Comput.* **2018**, *14*, 710–725.
- ²⁴ Kimber, P.; Plasser, F. Toward an understanding of electronic excitation energies beyond the molecular orbital picture *Phys. Chem. Chem. Phys.* **2020**, *22*, 6058–6080.
- Skomorowski, W.; Krylov, A. I. Real and imaginary excitons: Making sense of resonance wavefunctions by using reduced state and transition density matrices J. Phys. Chem. Lett. 2018, 9, 4101–4108.
- Meitner, L. About the β ray spectra and their connection with the γ radiation Z. Phys. 1922, 11, 35–54.
- ²⁷ Auger, P. Secondary β -rays produced in a gas by X-rays Comptes Rendus Acad. Sci. Paris **1923**, 177, 169.
- ²⁸ Cederbaum, L. S.; Zobeley, J.; Tarantelli, F. Giant intermolecular decay and fragmentation of clusters *Phys. Rev. Lett.* **1997**, *79*, 4778–4781.
- ²⁹ Zobeley, J.; Santra, R.; Cederbaum, L. S. Electronic decay in weakly bound heteroclusters:

- Energy transfer versus electron transfer J. Chem. Phys. 2001, 115, 5076–5088.
- ³⁰ Ku, A.; Facca, V. J.; Cai, Z.; Reilly, R. M. Auger electrons for cancer therapy—a review EJNMMI Radiopharm. Chem. 2019, 4, 27.
- Pirovano, G.; Jannetti, S. A.; Carter, L. M.; Sadique, A.; Kossatz, S.; Guru, N.; Demétrio De Souza França, P.; Maeda, M.; Zeglis, B. M.; Lewis, J. S.; Humm, J. L.; Reiner, T. Targeted brain tumor radiotherapy using an Auger emitter Clin. Cancer Res. 2020, 26, 2871–2881.
- Borbinha, J.; Vaz, P.; Di Maria, S. Dosimetric assessment in different tumour phenotypes with Auger electron emitting radionuclides: ^{99m}Tc, ¹²⁵I, ¹⁶¹Tb, and ¹⁷⁷Lu Radiat. Phys. Chem. **2020**, 172, 108763.
- ³³ Pirovano, G.; Wilson, T. C.; Reiner, T. Auger: The future of precision medicine Nucl. Med. and Bio. 2021, 96, 50–53.
- ³⁴ Skomorowski, W.; Krylov, A. I. Feshbach-Fano approach for calculation of Auger decay rates using equation-of-motion coupled-cluster wave functions. I. Theory and implementation *J. Chem. Phys.* 2021, 154, 084124.
- ³⁵ Ågren, H. On the interpretation of molecular valence Auger spectra J. Chem. Phys. 1981, 75, 1267–1283.
- Manne, R.; Ågren, H. Auger transition amplitudes from general many-electron wavefunctions Chem. Phys. 1985, 93, 201–208.
- ³⁷ Ågren, H.; Cesar, A.; Liegener, C.-M. Theory of molecular Auger spectra Adv. Quantum Chem. 1992, 23, 1–82.
- ³⁸ Cederbaum, L. S.; Domcke, W.; Schirmer, J. Many-body theory of core holes *Phys. Rev. A* 1980, 22, 206.
- ³⁹ Coriani, S.; Koch, H. Communication: X-ray absorption spectra and core-ionization potentials within a core-valence separated coupled cluster framework J. Chem. Phys. 2015, 143, 181103.
- ⁴⁰ Coriani, S.; Koch, H. Erratum: "Communication: X-ray absorption spectra and core-ionization potentials within a core-valence separated coupled cluster framework" [J. Chem. Phys. 143, 181103 (2015)] J. Chem. Phys. 2016, 145, 149901.
- Vidal, M. L.; Feng, X.; Epifanovsky, E.; Krylov, A. I.; Coriani, S. A new and efficient equation-of-motion coupled-cluster framework for core-excited and core-ionized states *J. Chem. Theory Comput.* 2019, 15, 3117–3133.
- ⁴² Vidal, M. L.: Krylov, A. I.: Coriani, S. Dyson orbitals within the fc-CVS-EOM-CCSD frame-

- work: theory and application to X-ray photoelectron spectroscopy of ground and excited states *Phys. Chem. Chem. Phys.* **2020**, *22*, 2693–2703.
- Skomorowski, W.; Krylov, A. I. Feshbach-Fano approach for calculation of Auger decay rates using equation-of-motion coupled-cluster wave functions. II. Numerical examples and benchmarks J. Chem. Phys. 2021, 154, 084125.
- ⁴⁴ Jayadev, N. K.; Ferino-Pérez, A.; Matz, F.; Krylov, A. I.; Jagau, T.-C The auger spectrum of benzene J. Chem. Phys. 2023, 158, 064109.
- Parravicini, V.; Jagau, T.-C. Interatomic and intermolecular Coulombic decay rates from equation-of-motion coupled-cluster theory with complex basis functions 2023; submitted; https://arxiv.org/abs/2305.10186.
- ⁴⁶ Epifanovsky, E.; Gilbert, A. T. B.; Feng, X.; Lee, J.; Mao, Y.; Mardirossian, N.; Pokhilko, P.; White, A. F.; Coons, M. P.; Dempwolff, A. L.; Gan, Z.; Hait, D.; Horn, P. R.; Jacobson, L. D.; Kaliman, I.; Kussmann, J.; Lange, A. W.; Lao, K. U.; Levine, D. S.; Liu, J.; McKenzie, S. C.; Morrison, A. F.; Nanda, K. D.; Plasser, F.; Rehn, D. R.; Vidal, M. L.; You, Z.-Q.; Zhu, Y.; Alam, B.; Albrecht, B. J.; Aldossary, A.; Alguire, E.; Andersen, J. H.; Athavale, V.; Barton, D.; Begam, K.; Behn, A.; Bellonzi, N.; Bernard, Y. A.; Berquist, E. J.; Burton, H. G. A.; Carreras, A.; Carter-Fenk, K.; Chakraborty, R.; Chien, A. D.; Closser, K. D.; Cofer-Shabica, V.; Dasgupta, S.; de Wergifosse, M.; Deng, J.; Diedenhofen, M.; Do, H.; Ehlert, S.; Fang, P.-T.; Fatehi, S.; Feng, Q.; Friedhoff, T.; Gayvert, J.; Ge, Q.; Gidofalvi, G.; Goldey, M.; Gomes, J.; González-Espinoza, C. E.; Gulania, S.; Gunina, A. O.; Hanson-Heine, M. W. D.; Harbach, P. H. P.; Hauser, A.; Herbst, M. F.; Hernández Vera, M.; Hodecker, M.; Holden, Z. C.; Houck, S.; Huang, X.; Hui, K.; Huynh, B. C.; Ivanov, M.; Jász, Á.; Ji, H.; Jiang, H.; Kaduk, B.; Kähler, S.; Khistyaev, K.; Kim, J.; Kis, G.; Klunzinger, P.; Koczor-Benda, Z.; Koh, J. H.; Kosenkov, D.; Koulias, L.; Kowalczyk, T.; Krauter, C. M.; Kue, K.; Kunitsa, A.; Kus, T.; Ladjánszki, I.; Landau, A.; Lawler, K. V.; Lefrancois, D.; Lehtola, S.; Li, R. R.; Li, Y.-P.; Liang, J.; Liebenthal, M.; Lin, H.-H.; Lin, Y.-S.; Liu, F.; Liu, K.-Y.; Loipersberger, M.; Luenser, A.; Manjanath, A.; Manohar, P.; Mansoor, E.; Manzer, S. F.; Mao, S.-P.; Marenich, A. V.; Markovich, T.; Mason, S.; Maurer, S. A.; McLaughlin, P. F.; Menger, M. F. S. J.; Mewes, J.-M.; Mewes, S. A.; Morgante, P.; Mullinax, J. W.; Oosterbaan, K. J.; Paran, G.; Paul, A. C.; Paul, S. K.; Pavošević, F.; Pei, Z.; Prager, S.; Proynov, E. I.; Rák, Á.; Ramos-Cordoba, E.; Rana, B.; Rask, A. E.; Rettig, A.; Richard, R. M.; Rob, F.; Rossomme, E.; Scheele, T.; Scheurer,

- M.; Schneider, M.; Sergueev, N.; Sharada, S. M.; Skomorowski, W.; Small, D. W.; Stein, C. J.; Su, Y.-C.; Sundstrom, E. J.; Tao, Z.; Thirman, J.; Tornai, G. J.; Tsuchimochi, T.; Tubman, N. M.; Veccham, S. P.; Vydrov, O.; Wenzel, J.; Witte, J.; Yamada, A.; Yao, K.; Yeganeh, S.; Yost, S. R.; Zech, A.; Zhang, I. Y.; Zhang, X.; Zhang, Y.; Zuev, D.; Aspuru-Guzik, A.; Bell, A. T.; Besley, N. A.; Bravaya, K. B.; Brooks, B. R.; Casanova, D.; Chai, J.-D.; Coriani, S.; Cramer, C. J.; Cserey, G.; DePrince, A. E.; DiStasio, R. A.; Dreuw, A.; Dunietz, B. D.; Furlani, T. R.; Goddard, W. A.; Hammes-Schiffer, S.; Head-Gordon, T.; Hehre, W. J.; Hsu, C.-P.; Jagau, T.-C.; Jung, Y.; Klamt, A.; Kong, J.; Lambrecht, D. S.; Liang, W.; Mayhall, N. J.; McCurdy, C. W.; Neaton, J. B.; Ochsenfeld, C.; Parkhill, J. A.; Peverati, R.; Rassolov, V. A.; Shao, Y.; Slipchenko, L. V.; Stauch, T.; Steele, R. P.; Subotnik, J. E.; Thom, A. J. W.; Tkatchenko, A.; Truhlar, D. G.; Van Voorhis, T.; Wesolowski, T. A.; Whaley, K. B.; Woodcock, H. L.; Zimmerman, P. M.; Faraji, S.; Gill, P. M. W.; Head-Gordon, M.; Herbert, J. M.; Krylov, A. I. Software for the frontiers of quantum chemistry: An overview of developments in the Q-Chem 5 package J. Chem. Phys. 2021, 155, 084801.
- ⁴⁷ Krylov, A. I.; Gill, P. M. W. Q-Chem: An engine for innovation WIREs: Comput. Mol. Sci. 2013, 3, 317–326.
- Depending on molecular orientation, symmetry labels corresponding to the same orbital or vibrational mode may be different. Q-Chem's standard molecular orientation is different from that of Mulliken? For example, Q-Chem would place water molecule in the xz plane instead of the yz. Consequently, for C_{2v} symmetry, b₁ and b₂ labels are flipped. More details can be found at http://iopenshell.usc.edu/resources/howto/symmetry/. To avoid confusion with different molecular orientations and relabeling the states, here we report the structures and symmetry labels following the Q-Chem's notations.
- ⁴⁹ Spohr, R.; Bergmark, T.; Magnusson, N.; Werme, L. O.; Nordling, C.; Siegbahn, K. Electron spectroscopic investigation of Auger processes in bromine substituted methanes and some hydrocarbons *Phys. Scr.* 1970, 2, 31.
- Rennie, E. E.; Kempgens, B.; Köppe, H. M.; Hergenhahn, U.; Feldhaus, J.; Itchkawitz, B. S.; Kilcoyne, A. L. D.; Kivimäki, A.; Maier, K.; Piancastelli, M. N.; Polcik, M.; Rüdel, A.; Bradshaw, A. M. A comprehensive photoabsorption, photoionization, and shake-up excitation study of the C1s cross section of benzene J. Chem. Phys. 2000, 113, 7362–7375.
- ⁵¹ Carniato, S.; Selles, P.; Ferté, A.; Berrah, N.; Wuosmaa, A. H.; Nakano, M.; Hikosaka, Y.; Ito,

- K.; Žitnik, M.; Bučar, K.; Soejima, K.; Jänkälä, K.; Cubaynes, D.; Bizau, J.-M.; Andric, L.; Khalal, M. A.; Palaudoux, J.; Lablanquie, P.; Penent, F. Single photon simultaneous K-shell ionization/excitation in C₆H₆: Experiment and theory J. Phys. B **2020**, 53, 244010.
- Nanda, K. D.; Vidal, M. L.; Faber, R.; Coriani, S.; Krylov, A. I. How to stay out of trouble in RIXS calculations within the equation-of-motion coupled-cluster damped response theory? Safe hitchhiking in the excitation manifold by means of core-valence separation *Phys. Chem. Chem. Phys.* 2020, 22, 2629–2641.
- Vidal, M. L.; Epshtein, M.; Scutelnic, V.; Yang, Z.; Xue, T.; Leone, S. R.; Krylov, A. I.; Coriani, S. The interplay of open-shell spin-coupling and Jahn-Teller distortion in benzene radical cation probed by x-ray spectroscopy J. Phys. Chem. A 2020, 124, 9532–9541.
- Kjellsson, L.; Nanda, K. D.; Rubensson, J.-E.; Doumy, G.; Southworth, S. H.; Ho, P. J.; March, A. M.; Al Haddad, A.; Kumagai, Y.; Tu, M.-F.; Debnath, T.; Bin Mohd Yusof, M. S.; Arnold, C.; Schlotter, W. F.; Moeller, S.; Coslovich, G.; Koralek, J. D.; Minitti, M. P.; Vidal, M. L.; Simon, M.; Santra, R.; Loh, Z.-H.; Coriani, S.; Krylov, A. I.; Young, L. Resonant inelastic x-ray scattering reveals hidden local transitions of the aqueous OH radical *Phys. Rev. Lett.* 2020, 124, 236001.